

# Ferroelectric-defined reconfigurable homojunctions for in-memory sensing and computing

Received: 17 April 2023

Accepted: 3 September 2023

Published online: 28 September 2023

 Check for updates

Guangjian Wu<sup>1,2,3,8</sup>, Xumeng Zhang<sup>1,2,3,8</sup>, Guangdi Feng<sup>4,8</sup>, Jingli Wang<sup>1</sup>, Keji Zhou<sup>1</sup>, Jinhua Zeng<sup>5</sup>, Danian Dong<sup>6</sup>, Fangduo Zhu<sup>1</sup>, Chenkai Yang<sup>4</sup>, Xiaoming Zhao<sup>4</sup>, Danni Gong<sup>4</sup>, Mengru Zhang<sup>1</sup>, Bobo Tian<sup>4</sup>✉, Chungang Duan<sup>4</sup>, Qi Liu<sup>1,2,3</sup>✉, Jianlu Wang<sup>1,2,3,7</sup>✉, Junhao Chu<sup>4,5,7</sup> & Ming Liu<sup>1,2,3</sup>

Recently, the increasing demand for data-centric applications is driving the elimination of image sensing, memory and computing unit interface, thus promising for latency- and energy-strict applications. Although dedicated electronic hardware has inspired the development of in-memory computing and in-sensor computing, folding the entire signal chain into one device remains challenging. Here an in-memory sensing and computing architecture is demonstrated using ferroelectric-defined reconfigurable two-dimensional photodiode arrays. High-level cognitive computing is realized based on the multiplications of light power and photoresponsivity through the photocurrent generation process and Kirchhoff's law. The weight is stored and programmed locally by the ferroelectric domains, enabling 51 (>5 bit) distinguishable weight states with linear, symmetric and reversible manipulation characteristics. Image recognition can be performed without any external memory and computing units. The three-in-one paradigm, integrating high-level computing, weight memorization and high-performance sensing, paves the way for a computing architecture with low energy consumption, low latency and reduced hardware overhead.

Traditional vision architecture involves a physically separated sensor, memory and processing units, where the shuttling of large amounts of raw data through the entire signal chain incurs notable energy consumption problems, time delays and hardware costs<sup>1</sup>. With the development of delay-strict applications and sensor-rich platforms, people pursue to eliminate the sensor, memory and processor interface in

disruptive architectures<sup>2–8</sup>. In-memory computing techniques that combine the memory and computing modules have been extensively boosted with the emergence of memristive materials<sup>9–11</sup>. In-sensor computing (ISC) techniques that combine the sensor and computing modules, inspired by multifunctional image sensors, have also been widely explored in recent years<sup>12–19</sup>. However, an architecture for the

<sup>1</sup>State Key Laboratory of Integrated Chips and Systems, Frontier Institute of Chip and System, Fudan University, Shanghai, China. <sup>2</sup>Shanghai Qi Zhi Institute, Xuhui District, Shanghai, China. <sup>3</sup>Zhangjiang Fudan International Innovation Center, Fudan University, Shanghai, China. <sup>4</sup>Key Laboratory of Polar Materials and Devices (MOE), Ministry of Education, Shanghai Center of Brain-inspired Intelligent Materials and Devices, Department of Electronics, East China Normal University, Shanghai, China. <sup>5</sup>State Key Laboratory of Infrared Physics, Shanghai Institute of Technical Physics, Chinese Academy of Sciences, Shanghai, China. <sup>6</sup>Key Laboratory of Microelectronic Devices & Integrated Technology, Institute of Microelectronics, Chinese Academy of Sciences, Beijing, China. <sup>7</sup>Institute of Optoelectronics, Shanghai Frontier Base of Intelligent Optoelectronics and Perception, Fudan University, Shanghai, China. <sup>8</sup>These authors contributed equally: Guangjian Wu, Xumeng Zhang, Guangdi Feng. ✉e-mail: [bttian@ee.ecnu.edu.cn](mailto:bttian@ee.ecnu.edu.cn); [qi\\_liu@fudan.edu.cn](mailto:qi_liu@fudan.edu.cn); [jianluwang@fudan.edu.cn](mailto:jianluwang@fudan.edu.cn)

in-memory sensing and computing (IMSC) paradigm that combines all three modules has not yet been developed.

To date, a variety of neuromorphic vision sensors emulating specific functions of the human retina have been designed to implement in situ vision pre-processing<sup>20–28</sup>. The optimization of raw data can substantially accelerate the subsequent computing process. However, ‘computing’ here is a signal pre-processing process, which still relies on the external post-processing for image recognition. It is more appropriate to call it a ‘pre-processing’ process rather than a ‘computing’ process, as the output is still the representation of the input signal. To realize image perception and recognition, high-level ISC based on matrix–vector multiplication (MVM) operations should be performed, where positive and negative weights are prerequisites. This issue is currently being pursued urgently, for example, source–drain voltages (which can be negative), or fake negative weights from subtraction have been employed as artificial neural network (ANN) weights<sup>4,29</sup>. This is impractical as the array needs scaling up due to the power consumption and hardware area problems. Another issue for the high-level ISC is the stored weights in an external memory, which inevitably incurs additional power consumption and scalability obstacles<sup>3,30</sup>. Due to the above problems, a three-in-one IMSC paradigm, integrating high-performance sensing, weight storage and high-level computing, is desired but has not been realized.

Here a reconfigurable two-dimensional (2D) photodiode array with weight stored locally in the coupling ferroelectric gate dielectrics is demonstrated to enable IMSC, where sensitive image sensing, weight memorization and high-level computing capabilities are integrated into the sensor arrays. Also, 2D semiconductor p and n doping is accessible using ferroelectric polarization<sup>31</sup>; thus, a p–n homojunction can be constructed at the antagonism ferroelectric field interface. The potential profile of the homojunction and thus the photoresponsivity can be tuned by the ferroelectric field. The band alignment evolution from a p–n junction to an n–p junction produces intrinsic positive and negative photoresponsivities<sup>32,33</sup>, simplifying the hardware overhead for the ANN. The devices display nearly ideal characteristics for IMSC in terms of several factors, including high-level computing (showing positive and negative weights with linear, symmetric and reversible manipulation characteristics), memory (showing photoresponsivity memory ability) and high-performance sensing (showing broadband, fast and sensitive photosensing ability). Based on these characteristics, an in situ MVM operation for simultaneous image sensing and processing is performed, and three distinct image features are experimentally obtained via a one-step convolution operation using the three-in-one kernels. In addition, the ferroelectric-defined photodiode arrays are trained to carry out pattern recognition and classification tasks to command the movement of a robot dog without any external memory or computing units. The reconfigurable 2D photodiodes with locally ferroelectric-stored weights consume zero energy at the sensor-array level, reduce the latency and simplify the hardware complexity substantially, providing a brand new inspiration to build IMSC systems.

The vast majority of the state-of-the-art ISC works are based on emerging sensors with adaptive characteristics for image pre-processing<sup>2,34–36</sup>, whereas our reconfigurable sensors, equipped with tunable positive and negative weights, can constitute themselves as an ANN for high-level cognitive computing. Few high-level ISC works have been reported until now<sup>3,30</sup>. Compared with them, the advance of our work is the introduction of the local weight storage function to enable the IMSC paradigm, further accelerating the development of computing architecture with low latency, low power consumption and reduced hardware overhead.

## Flows of different sensory computing architectures

In the conventional computing architecture (Fig. 1a), a large amount of raw and unstructured data have to be transferred through the entire

signal chain, resulting in high latency and inefficient power consumption. By incorporating memory and computing into one module, in-memory computing blurs the boundary between memory and processing units<sup>37</sup>, as the sensor arrays remain unchanged. It is natural to put forward an idea that enduing the in-memory computing paradigm with image-sensing ability to realize IMSC, where sensing and computing tasks take place simultaneously with weights stored in local memory. However, naturally non-volatile materials, such as memristive materials and ferroelectrics, are not qualified for high-performance photodetection. Conventional high-performance photodetectors are based on the p–n junction structure, allowing sensitive and ultrafast image sensing<sup>38</sup>. Here we combine the advantages of junction structures in photodetection with those of ferroelectrics in weight storage to realize an IMSC system (Fig. 1b). The band profile of 2D materials can be switched between p–n and n–p junctions, giving rise to positive and negative photoresponsivities. The non-volatile weight storage ability (namely, the ability to store a linear continuous photoresponsivity  $R$ ) facilitates the core-computing primitive of analogue MVM. The photocurrent generation process ( $I_{ph} = P \times R$ ) and Kirchhoff’s current summation laws are exploited to realize this operation, where  $I_{ph}$  denotes the output photocurrent and  $P$  represents the incident illumination power. Images can be directly recognized through the IMSC chip without any external memory or processing units, thereby achieving time and energy efficiency.

## Ferroelectric-defined 2D homojunctions for IMSC

A 2D material MoTe<sub>2</sub> homojunction defined by a ferroelectric is constructed to perform the IMSC operation (Fig. 2a), where a robust organic ferroelectric poly(vinylidene fluoride) and trifluoroethylene (P(VDF-TrFE)) is employed as the weight-storage gate dielectric. The split gates beneath the dielectric (Gate1 and Gate2) are used to independently manipulate the ferroelectric domains on the left and right sides. Graphene is introduced for ohmic contacts<sup>39</sup>, with the resulting Raman spectra indicating the high-quality crystal structure (Supplementary Fig. 1). The detailed device fabrication process is presented in Methods and Supplementary Fig. 2. A p–n/n–p junction is constructed when the left and right regions of the ferroelectric gate dielectric are fully polarized oppositely, corresponding to the largest negative/positive photoresponsivity. The ferroelectric domains can be gradually switched by applying a voltage pulse to the split gates, resulting in a reduction in the junction built-in electric field and hence the photoresponsivity. Therefore, the intermediate-photoresponsivity states can be acquired by manipulating the ferroelectric domain configurations. Supplementary Fig. 3 shows the evolution of the junction potential profile with ferroelectric polarization. The high-resolution transmission electron microscopy and energy-dispersive X-ray spectroscopy elemental mapping images demonstrate clean interfaces, enabling efficient ferroelectric-field regulation and charge transportation (Fig. 2b).

When connecting the split gates with the metal wire, gate voltage  $V_g$  is set equal to that of Gate1 ( $V_{g1}$ ) and Gate2 ( $V_{g2}$ ). In this condition, the device is a simple ferroelectric field-effect transistor, and the transfer curve shows typical ferroelectric hysteresis (Fig. 2c). The positive and negative ferroelectric switching currents  $I_g$  are approximately equal, indicating the negligible imprint effect and a coercive voltage of 13 V (ref. 28). The coercive voltage can be substantially reduced by reducing the P(VDF-TrFE) thickness, which maintains its ferroelectric properties even when scaled down to a few nanometres<sup>40</sup>. The output curve (source–drain current  $I_{sd}$  versus source–drain voltage  $V_{sd}$ ) demonstrates four distinct configurations under different ferroelectric polarization states (Fig. 2d). When the left/right sides of P(VDF-TrFE) are polarized up/down, a p–n homojunction with a high current rectification beyond  $10^4$  and negligible reverse current is constructed. Conversely, when the left/right sides of P(VDF-TrFE) are polarized down/up, the device is reversed to the n–p configuration. For simplicity, only voltage pulse  $V$  applied to the left gate is given below, unless otherwise

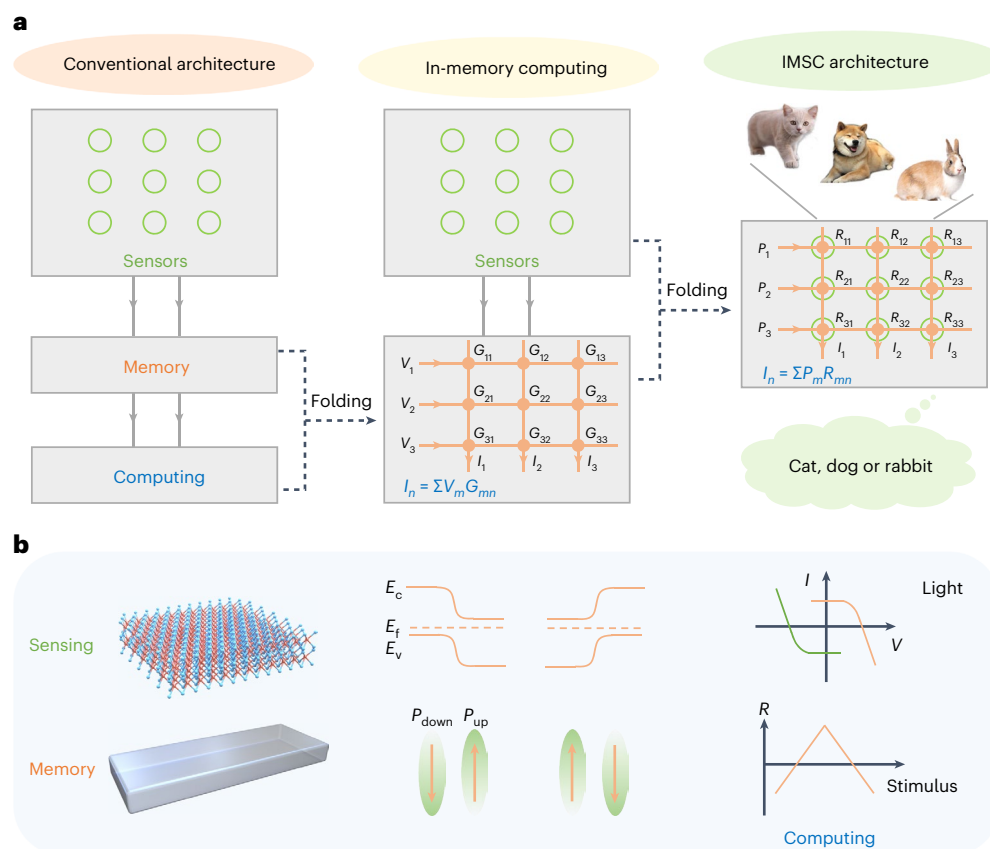


**Fig. 1 | Different sensory computing architectures and schematic of proposed IMSC architectures.** **a**, Left: flow for conventional sensory computing architecture with separate sensing, memory and computing units. Middle: in-memory computing architecture with folded memory and computing units. Right: schematic of the IMSC architectures, integrating image sensing, weight memorization and computing modules. Image recognition can be directly realized through the IMSC chip without any external memory and processing,

demonstrating time and energy efficiency. **b**, Design of ferroelectric-defined reconfigurable 2D homojunctions for IMSC. The advantages of junction structure in photodetection and that of ferroelectric in weight memorization are combined together to realize IMSC systems.  $E_c$ ,  $E_f$  and  $E_v$  are the conduction band edge, Fermi level and valence band edge, respectively.  $P_{\text{down}}$  and  $P_{\text{up}}$  represent the ferroelectric polarization-down and polarization-up states, respectively.

specified (an equal but opposite  $-V$  is simultaneously applied to the right gate). When both sides are polarized up/down, the nn/pp configuration with a linear and symmetric output curve is obtained. Figure 2e verifies the ferroelectric-defined intermediate junction states from a total n-p junction (state I) to a p-n junction (state VII). Supplementary Fig. 4 illustrates the detailed pulse voltage operation configuration and the corresponding phase differences in the piezoresponse force microscopy data. The gradual transformation from an n-p to a p-n homojunction verifies the intermediate potential profiles defined by the ferroelectric domains, which are responsible for the linear and continuous photoresponsivity tunability process.

Under illumination, both ferroelectric-defined p-n and n-p junctions generate an obvious open-circuit voltage and short-circuit photocurrent  $I_{\text{sc}}$  arising from the photovoltaic effect, where the p-n/n-p junction produces a negative/positive photocurrent (Fig. 3a). This is absent in pp and nn junctions, implying that the origin of the photocurrent is the p-n junction interface rather than the Schottky junction<sup>32</sup>. This result is verified by the spatially scanning photocurrent mapping images (Supplementary Fig. 5). In particular, the photocurrent is almost equal in amount in the p-n and n-p junctions with the same but opposite polarization configurations. Compared with the gating-induced photoresponsivity tunability where voltage magnitudes are required to change<sup>4,30</sup>, the symmetrical voltage operation scheme can simplify the hardware implementation. The photoresponsivity  $R$  reaches  $830 \text{ mA W}^{-1}$  when the bias voltage is 0 V. The external

quantum efficiency (EQE) is calculated as  $\text{EQE} = (I_{\text{sc}}/P_{\text{in}}) \times (hc/e\lambda)$ , where  $P_{\text{in}}$ ,  $h$ ,  $\lambda$  and  $c$  are the incident light power, Planck's constant, light wavelength and speed of light, respectively<sup>39</sup>. An EQE constant of ~6% is obtained for the ferroelectric-defined p-n homojunction. Here the  $R$  and EQE values are better than those of 2D homojunctions tuned by the external electrostatic field<sup>32,38</sup>. Our photodetector consumes zero energy after programming due to the non-volatile weight storage ability and self-power photogeneration process. When the ferroelectric configurations are manipulated from state I to state VII, the photocurrent gradually changes from negative to positive as the band alignment evolves from a p-n to an n-p potential profile (Fig. 3b).

More intermediate-photoresponsivity states, between the p-n and n-p junctions, can be obtained by applying a series of pulse voltages (Supplementary Fig. 6). The corresponding photoresponsivity changes linearly and continuously from  $-800$  to  $+800 \text{ mA W}^{-1}$  (Fig. 3c). By reversing the voltage pulse polarity, the photoresponsivity varies inversely from  $+800$  to  $-800 \text{ mA W}^{-1}$ . Benefiting from the gradually switching ferroelectric domains, both long-term potentiation (LTP) and long-term depression (LTD) processes of photoresponsivity contain 51 distinguishable states (more than five bits), which is, to the best of our knowledge, the most accessible  $R$  levels from negative to positive region to date. The photoresponsivity is linearly proportional to the number of voltage pulses, as demonstrated by the device nonlinearity model (Methods). The nonlinearity value for LTP/LTD process is  $0.12/-0.12$  (Supplementary Fig. 6) ( $0/0$  is the ideal value), which is

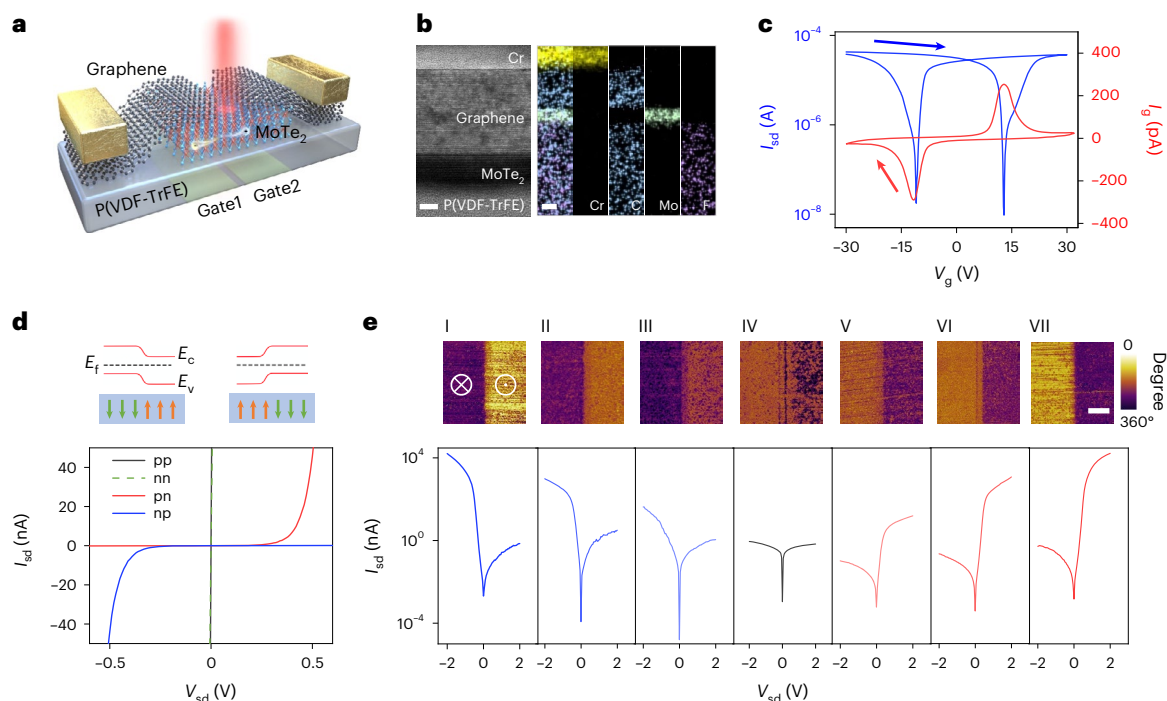


**Fig. 2 | Ferroelectric-defined reconfigurable 2D homojunctions.**

**a**, Schematic of the ferroelectric-defined reconfigurable 2D homojunctions. **b**, High-resolution transmission electron microscopy and energy-dispersive X-ray spectroscopy elemental mapping images of the device. Scale bars, 5 nm (left) and 10 nm (right). **c**, Transfer characteristic (blue line) and  $I_g$ - $V_g$  curve (red line) with  $V_{sd} = 1$  V when connecting the split gates, demonstrating typical ferroelectric hysteresis. **d**, Output characteristics with the corresponding band diagram

under different ferroelectric polarization configurations. A +35/-35 V voltage pulse with a pulse width of 10 ms is used to polarize the P(VDF-TrFE) up/down. **e**, Gradual transformation from n-p to p-n homojunctions defined by ferroelectric domains. Top: piezoresponse force microscopy phase images for different polarization conditions. Bottom: the corresponding output characteristics of the homojunction. The dot/cross in a circle indicates the ferroelectric domains in the polarization-up/polarization-down state. Scale bar, 1  $\mu$ m.

much better than the conductance linearity of the reported emerging non-volatile memory<sup>41</sup>. The small nonlinearity, symmetric LTP/LTD processes and negligible cycle-to-cycle variation are essential for high image recognition accuracy<sup>42</sup>. The multiple levels of positive and negative photocurrents show uniform steps and non-overlapping regions (Fig. 3d), verifying the stable and continuous photocurrent tunability using ferroelectric domains.

In addition to linear  $R$  regulation, the linear light intensity dependence of the photocurrent is crucial for processing grey-scale images, which is a cumbersome task for scenarios involving nonlinear power-dependent photocurrent, such as trapping-induced photoresponse<sup>4</sup>. The dependence of the photocurrent on illumination power for the seven states shown in Fig. 2e is extracted in Fig. 3e, where the linear fitting curves with the formula  $I_{ph} \propto P^\alpha$  are also demonstrated. The values of  $\alpha$  are 1.15, 1.04, 0.87, 0.80, 1.13, 1.00 and 0.86 (close to the ideal value of 1.00) for states I to VII, respectively, demonstrating linear correlations. Figure 3f presents the long-term stability of 17 distinct photoresponsivity states (eight positive states, eight negative states and one 'zero' state), where the photoresponsivity remains nearly unchanged over 1,000 s. Supplementary Fig. 7 shows a much longer retention time of 24 h and the long-term stability of all the 51 photoresponsivity states. Another prerequisite for IMSC is the endurance characteristics (Fig. 3g). Both positive and negative photocurrents demonstrate negligible deterioration after  $10^6$  cycles, which is consistent with the results of the P(VDF-TrFE) capacitor structure (Supplementary Fig. 8). Figure 3h illustrates the wavelength-dependent positive and negative photoresponses, covering the ultraviolet (340 nm) to near-infrared (1,310 nm) range. This indicates the potential of the device in broadband convolutional processing<sup>30</sup>. Benefiting from the photovoltaic effects, the ferroelectric-defined homojunction exhibits

a fast photoresponse with a rising time of 1.9  $\mu$ s and a decay time of 0.6  $\mu$ s (Supplementary Fig. 9), which is essential for ultrafast image recognition. The programming voltage amplitude could be reduced by decreasing the ferroelectric thickness. Supplementary Fig. 10 shows the results, together with the endurance and retention properties.

## Reconfigurable homojunction array for IMSC

Based on the ferroelectric-stored multiple states of photoresponsivity and the sensitive photodetection capabilities, IMSC implementation can be carried out using the reconfigurable sensor array. An image sensor with  $3 \times 3$  pixels is constructed (Fig. 4a), where each pixel comprises three subpixels (one subpixel is an individual ferroelectric tunable homojunction), as marked by the square frames. The three subpixels in the one-pixel design can greatly simplify the image acquisition process. Here  $R_{mn}$  is used to represent the photoresponsivity of the diode, where  $m$  and  $n$  are the corresponding pixel and subpixel indices ( $m = 1, 2, \dots, 9$ ;  $n = 1, 2, 3$ ). The first ( $n = 1$ ), second ( $n = 2$ ) and third ( $n = 3$ ) subpixel in each square are the element in Array 1 (red square), Array 2 (blue square) and Array 3 (green square), respectively. The spatially staggered arrangement of the three  $3 \times 3$  sensor arrays enables a three-in-one convolution kernel; thus, three distinct image features can be simultaneously obtained in one convolution operation. The MVM operation can be carried out by summing all the photocurrents in the  $n$ th sensor array, and the output photocurrent vector of each sensor array  $\mathbf{I}_n$  can be expressed as

$$\mathbf{I}_n = \mathbf{R}_{mn} \times \mathbf{P}_m = \begin{bmatrix} I_1 \\ I_2 \\ I_3 \end{bmatrix} = \begin{bmatrix} R_{11} & R_{21} & \cdots & R_{91} \\ R_{12} & R_{22} & \cdots & R_{92} \\ R_{13} & R_{23} & \cdots & R_{93} \end{bmatrix} \begin{bmatrix} P_1 \\ \vdots \\ P_9 \end{bmatrix}$$



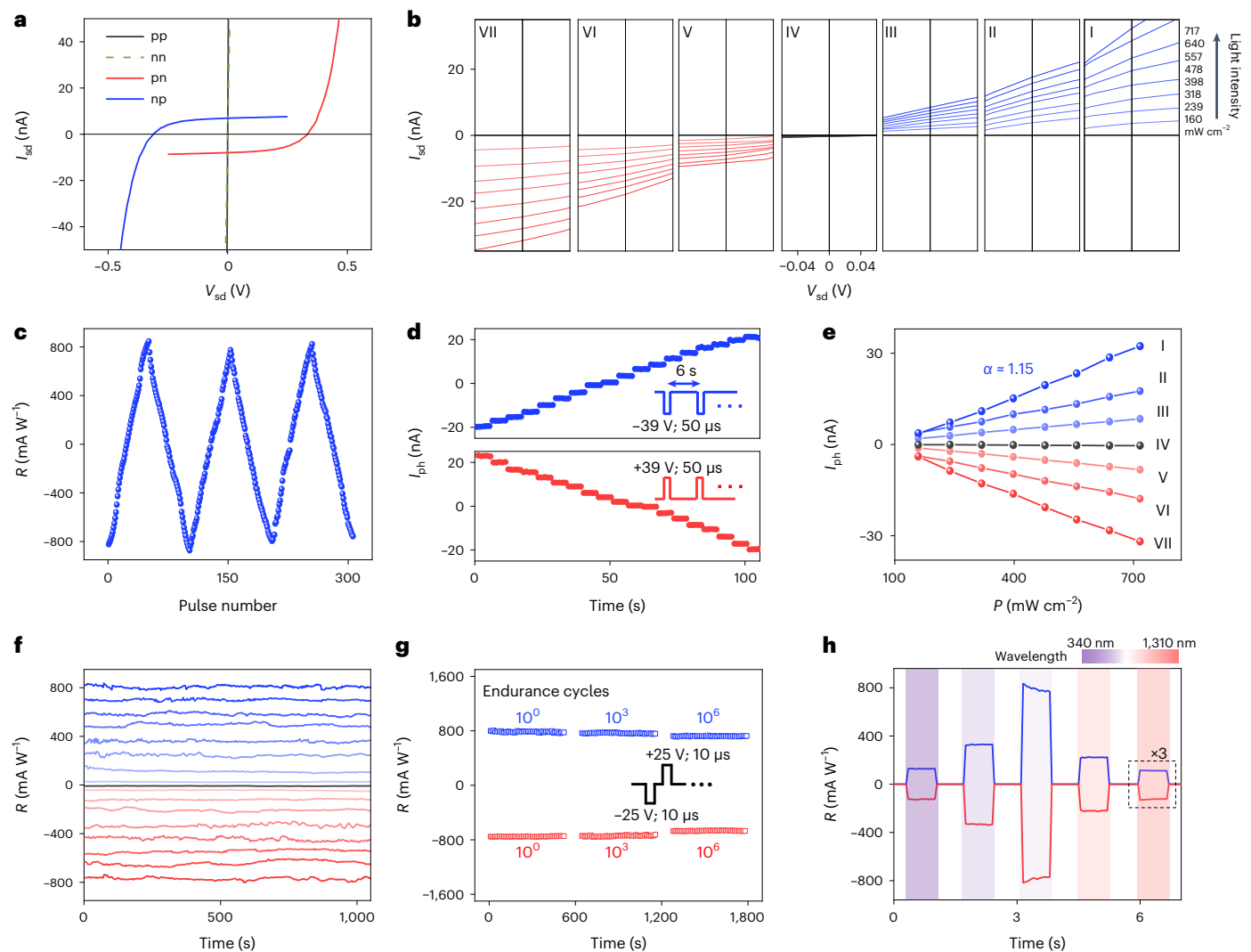


**Fig. 3 | Optoelectronic properties of the weight-reconfigurable 2D homojunctions.** **a**, Photoresponse of the device under different ferroelectric polarization configurations with an illumination intensity of  $240 \text{ mW cm}^{-2}$ . **b**,  $I_{\text{sd}}-V_{\text{sd}}$  curves of homojunctions under different illumination powers, consistent with the seven states from p-n to n-p junctions shown in Fig. 2e. **c**, Three-cycle photoresponsivity LTP and LTD characteristics tuned by ferroelectric domains. **d**, Multiple levels of cumulative positive and negative photocurrents with uniform increments and non-overlapping regions. The light pulse duration is  $50 \mu\text{s}$  with a  $6 \text{ s}$  interval (inset). **e**, Dependence of

photocurrents on different illumination powers for the seven states shown in Fig. 2e. **f**, Long-term stability of eight positive states, eight negative states and one 'zero' state. **g**, Positive and negative photocurrents after different endurance pulse cycles, demonstrating negligible deterioration. The positive and negative photocurrents are recorded after endurance pulse cycles, which consist of voltage pulses with amplitudes of  $+25$  and  $-25 \text{ V}$  and a pulse width of  $10 \mu\text{s}$ . **h**, Wavelength-dependent positive and negative photoresponses of the ferroelectric-defined homojunction, covering the ultraviolet to near-infrared regimes. The incident wavelengths are  $340$ ,  $520$ ,  $637$ ,  $940$  and  $1,310 \text{ nm}$ .

where  $P_m$  is the illumination power incident on the  $m$ th pixel. The photoresponsivity of the individual subpixels can be updated and stored by the ferroelectric domains during the training process. Hence, image sensing, weight storage and MVM operation are simultaneously realized in the ferroelectric-defined sensor array. Here transferred gold (Au) electrodes are employed instead of graphene to enable scalable electrode preparation with minimal interfacial disorder<sup>33</sup>, demonstrating approximately the same electrical characteristics (Supplementary Fig. 11). Methods presents the detailed array fabrication process. Figure 4b presents the weight distribution histogram of the photodiode in the sensor array with 13 well-separated photoresponsivity states. The Raman spectra and  $R$  distribution of all the devices in the array show good uniformity and ferroelectric tunability (Supplementary Figs. 12 and 13). The photo-current accumulation process is confirmed (Supplementary Fig. 14).

Based on the layout of the ferroelectric weight memorization array, image sensing and processing can be simultaneously realized.

By individually adjusting the weight of each subpixel, various types of convolution kernel can be constructed. Figure 4c demonstrates the original grey-scale image and illustration of three-in-one kernels. Here three kernels with right edge detection, top edge detection and sharpen functions are fabricated using Array 1, Array 2 and Array 3, respectively (Supplementary Fig. 15). Figure 4d illustrates the actual  $R$  configurations in the three kernels. Due to the staggered spatial arrangement of the array, the corresponding three image features can be simultaneously acquired through one convolution cross-correlation operation (Fig. 4e). The key image features obtained from the original image are effectively consistent with the simulation results. Furthermore, a feature map of the edges can be obtained by combining the right and top edge detection results (Supplementary Fig. 16). The multiple convolution kernels based on the proposed reconfigurable sensor array can be used in a convolutional neural network for image recognition (Supplementary Fig. 17).

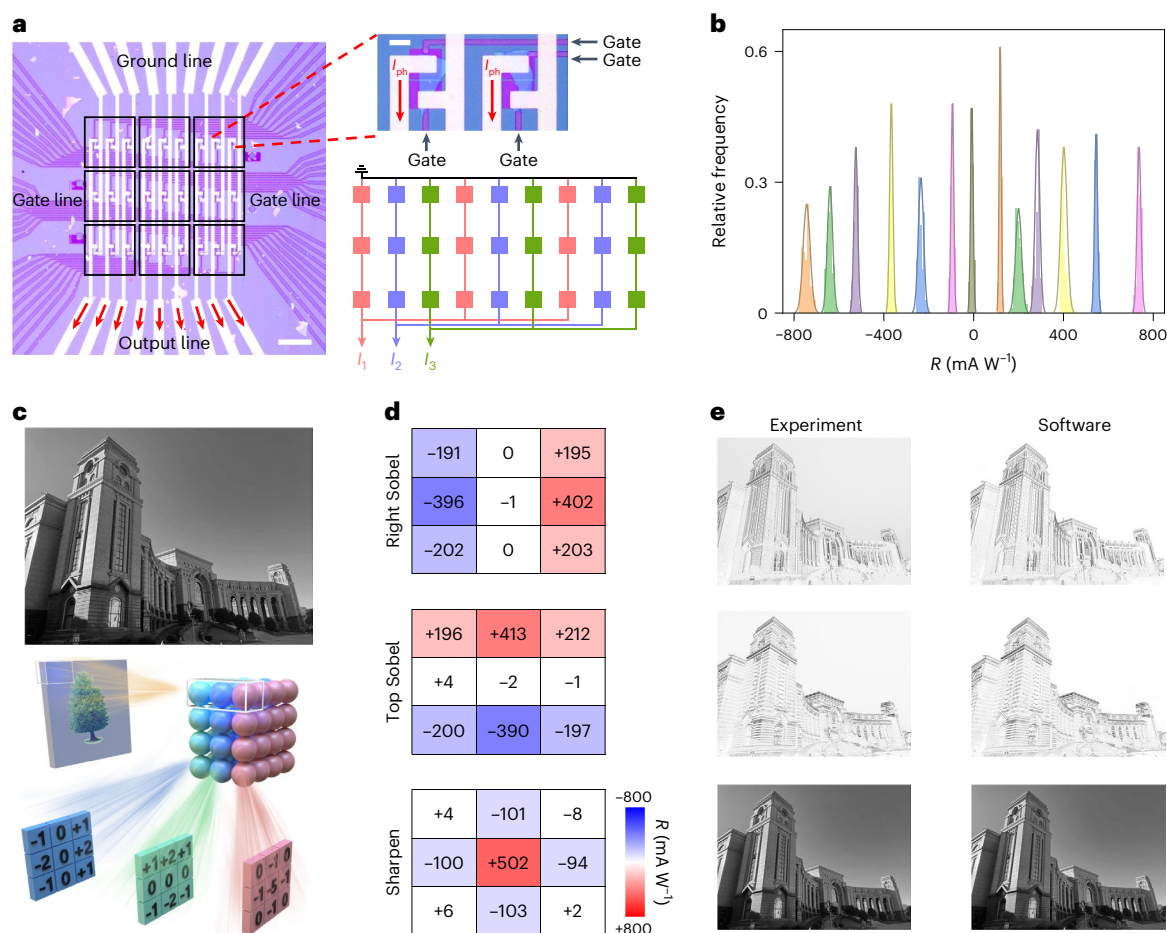


**Fig. 4 | Ferroelectric-defined weight-reconfigurable sensor array.**

**a**, Microscopy image of the ferroelectric-defined weight-reconfigurable MoTe<sub>2</sub> sensor array, consisting of 3 × 3 pixels. Scale bar, 100 μm. The magnified image is the optical microscopy image of two MoTe<sub>2</sub> phototransistor subpixels. Scale bar, 10 μm. The bottom-right corner shows a schematic of the photodiode array. The red, blue and green devices are the subpixels of Array 1, Array 2 and Array 3, respectively.

respectively. **b**, Weight distribution histogram of one photodiode in the sensor array with well-separated 13 photoresponsivity states. **c**, Original grey-scale image (top) and illustration of the three-in-one kernels (bottom). **d**, Actual  $R$  configurations in three kernels to perform parallel edge detection, representing right, top and sharpen Sobels. **e**, Experiment and software edge detection results using the ferroelectric-defined weight-reconfigurable kernels.

The reconfigurable sensor array with local weight storage capability can also itself act as an ANN to directly classify patterns without any external memory or processing units, thereby eliminating the sensor and processor interface with zero latency and low power consumption. By pairing the IMSC chip with a wireless data transmission module, patterns can be recognized in real time and sent to a robot dog to perform the assigned actions (Fig. 5a). Supplementary Fig. 18 shows the detailed communication process between the IMSC chip and robot dog. Here a classification task was performed using 'L', 'J' and 'T' patterns, which were assigned to command the robot dog to turn left, turn right and stop, respectively (Fig. 5b). These patterns were projected onto the sensor array through masks (Supplementary Fig. 19). Photodiodes beneath the transparent areas of the masks were used to produce photocurrents through the network (Fig. 5b), whereas the shielded photodiodes produce zero photocurrents. The weights were trained by the backpropagation algorithm according to the discrepancy between the photocurrents produced by the array and target values. The mean square error between the real and predicted photocurrents was negligible after ten offline training epochs (Fig. 5c), and the corresponding weights were written into our array for pattern classification (Fig. 5d). Supplementary Fig. 20 shows the detailed training process. The IMSC chip acts as the eyes and brain of the robot dog, controlling the dog to turn left, turn

right and stop when the patterns 'L', 'J' and 'T' are observed, respectively. This control approach allows the robot dog to navigate along a zigzag track (Fig. 5e and Supplementary Video 1). The real-time output currents of the IMSC chip for the corresponding patterns are substantially larger than those for the other patterns, enabling the identification of the target image (Fig. 5f). The photocurrents are also well separated when noise is introduced into the projected patterns (Supplementary Fig. 21).

Supplementary Fig. 22 presents a comparison between our devices and different neuromorphic vision sensors. In particular, during the inference process, zero energy is consumed at the sensor-array level due to its self-power and non-volatile abilities. Moreover, in the programming process, our device consumes little power (10<sup>-13</sup> J), similar to that of a bioinspired visual system (10<sup>-15</sup>–10<sup>-13</sup> J per operation)<sup>43</sup>. Besides, Supplementary Fig. 23 demonstrates the difference in the operating frequency of IMSC computing compared with the conventional sensory computing architecture. Combined with advances in the ongoing wafer-scale integration of metal electrodes and 2D materials<sup>44,45</sup>, the proposed sensor array has the potential to be scaled to realize more complicated tasks.

Moreover, memory here refers to the ability of the device to store the weights (photoresponsivity  $R$ ) rather than the photocurrents (representing the incident light power  $P$ ), where  $I_{ph} = R \times P$ . It is similar

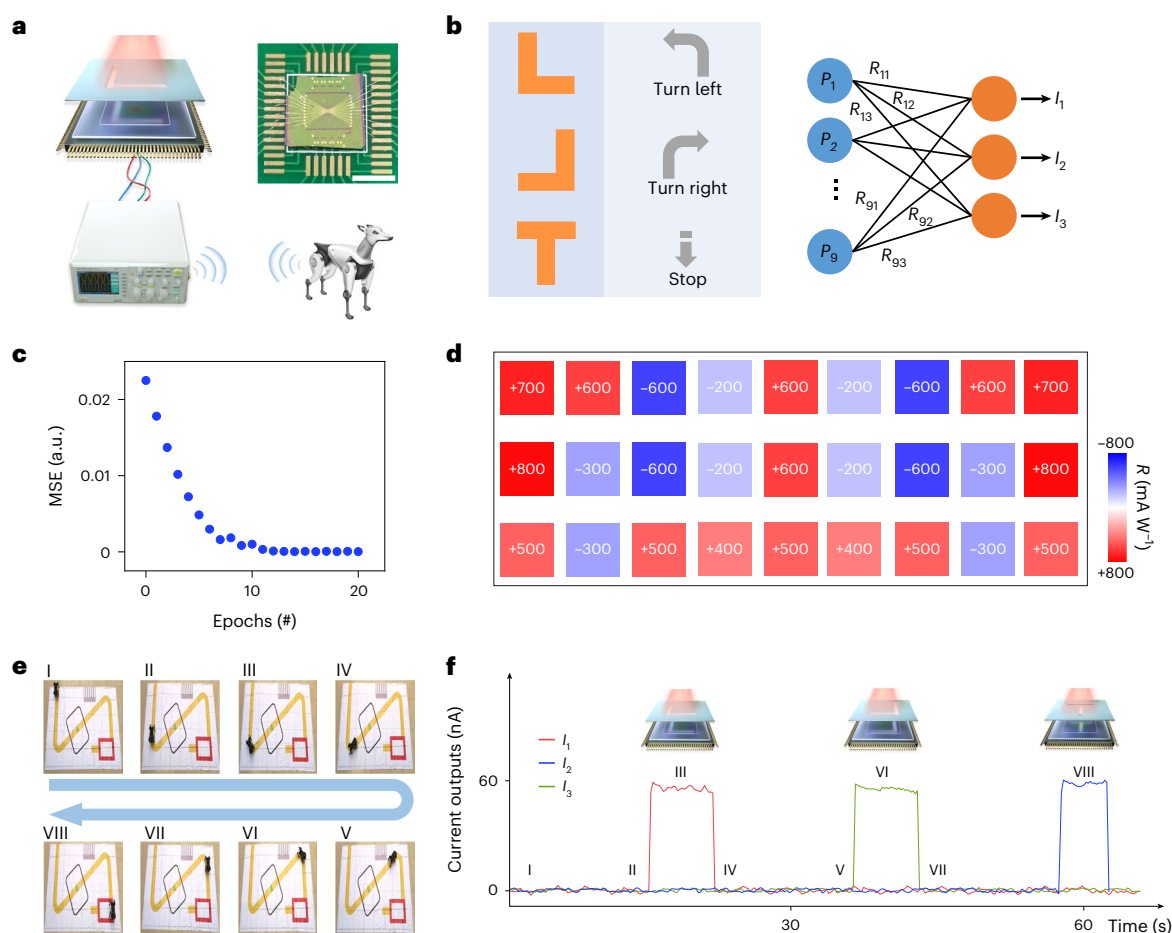


**Fig. 5 | Hardware implementation of image recognition using the ferroelectric-defined weight-reconfigurable sensor array.** **a**, Illustrations of the hardware implementation process. The incoming patterns are recognized by the IMSC chip, followed by a corresponding instruction to command the robot dog through a wireless signal. Scale bar, 5 mm. **b**, Patterns 'L', 'J' and 'T' are assigned to command the robot dog to move left, right and stop, respectively. Array 1 ( $I_1$ ), Array 2 ( $I_2$ ) and Array 3 ( $I_3$ ) are trained to identify patterns 'L', 'T' and 'J' through the ANN, respectively. **c**, Mean square error (MSE) between the real

and predicted photocurrents. **d**, Final weight distribution of the IMSC chip for classification tasks. **e**, Robot dog navigation using the IMSC chip. The motion trajectory of the robot dog is determined by the corresponding real-time current profiles, as shown in **f**. **f**, Real-time output currents of Array 1, Array 2 and Array 3 from time I to VIII, where current for the target pattern is well separated with those for the other patterns. If the output current of Array 1 ( $I_1$ ) is the largest, the ANN determines that the incoming pattern is 'L', and a 'turn left' instruction is sent to the robot dog. The illumination intensity is  $400 \text{ mW cm}^{-2}$ .

to that for in-memory computing ( $I_{\text{output}} = G \times V$ ), where weight conductance  $G$  is stored rather than input  $V$  (ref. 46). However, the claimed 'memory' ability in existing neuromorphic sensors basically refers to the storage of photocurrent, which can be applied for some signal pre-processing operations<sup>14</sup>. Nevertheless, these devices can hardly be used for high-level computing tasks because the weight  $R$  is changed when the photocurrent is stored, and reset operations are required before the next computing cycle.

## Outlook

We demonstrated a ferroelectric-defined reconfigurable sensor array to realize the IMSC paradigm, integrating high-performance image sensing, weight memorization and high-level computing together. A  $\text{MoTe}_2$  homojunction is constructed by using ferroelectric domains, and the potential profile can be continuously tuned from p–n (negative photoresponsivity) to n–p (positive photoresponsivity) junctions. The gradually switching ferroelectric domains allow linear, symmetric and multistate photoresponsivity regulation, effectively improving the image recognition accuracy. The photodiode array is implemented as multiple convolution kernels in a convolutional neural network for image recognition, and constitutes itself as an ANN for pattern classification without power consumption. The combination of the sensing

ability due to the junction structure and memorization capability due to the ferroelectric domains demonstrates that our array can be potentially applied as an efficient hardware in intelligent sensory systems.

## Online content

Any methods, additional references, Nature Portfolio reporting summaries, source data, extended data, supplementary information, acknowledgements, peer review information; details of author contributions and competing interests; and statements of data and code availability are available at <https://doi.org/10.1038/s41563-023-01676-0>.

## References

1. Zhou, F. & Chai, Y. Near-sensor and in-sensor computing. *Nat. Electron.* **3**, 664–671 (2020).
2. Zhou, F. et al. Optoelectronic resistive random access memory for neuromorphic vision sensors. *Nat. Nanotechnol.* **14**, 776–782 (2019).
3. Mennel, L. et al. Ultrafast machine vision with 2D material neural network image sensors. *Nature* **579**, 62–66 (2020).
4. Wang, C. Y. et al. Gate-tunable van der Waals heterostructure for reconfigurable neural network vision sensor. *Sci. Adv.* **6**, eaba6173 (2020).

5. Dodda, A., Trainor, N., Redwing, J. M. & Das, S. All-in-one, bio-inspired, and low-power crypto engines for near-sensor security based on two-dimensional memtransistors. *Nat. Commun.* **13**, 3587 (2022).
6. Rehman, S., Khan, M. F., Kim, H. D. & Kim, S. Analog-digital hybrid computing with SnS<sub>2</sub> memtransistor for low-powered sensor fusion. *Nat. Commun.* **13**, 2804 (2022).
7. Chai, Y. In-sensor computing for machine vision. *Nature* **579**, 32–33 (2020).
8. Chen, J. et al. Optoelectronic graded neurons for bioinspired in-sensor motion perception. *Nat. Nanotechnol.* **18**, 882–888 (2023).
9. Yao, P. et al. Fully hardware-implemented memristor convolutional neural network. *Nature* **577**, 641–646 (2020).
10. Jung, S. et al. A crossbar array of magnetoresistive memory devices for in-memory computing. *Nature* **601**, 211–216 (2022).
11. Kiani, F., Yin, J., Wang, Z., Yang, J. J. & Xia, Q. A fully hardware-based memristive multilayer neural network. *Sci. Adv.* **7**, eabj4801 (2021).
12. Choi, C. et al. Reconfigurable heterogeneous integration using stackable chips with embedded artificial intelligence. *Nat. Electron.* **5**, 386–393 (2022).
13. Lee, S., Peng, R., Wu, C. & Li, M. Programmable black phosphorus image sensor for broadband optoelectronic edge computing. *Nat. Commun.* **13**, 1485 (2022).
14. Zhang, Z. et al. All-in-one two-dimensional retinomorph hardware device for motion detection and recognition. *Nat. Nanotechnol.* **17**, 27–32 (2022).
15. Jang, H. et al. An atomically thin optoelectronic machine vision processor. *Adv. Mater.* **32**, e2002431 (2020).
16. Seo, S. et al. Artificial optic-neural synapse for colored and color-mixed pattern recognition. *Nat. Commun.* **9**, 5106 (2018).
17. Zhu, Q. B. et al. A flexible ultrasensitive optoelectronic sensor array for neuromorphic vision systems. *Nat. Commun.* **12**, 1798 (2021).
18. Moin, A. et al. A wearable biosensing system with in-sensor adaptive machine learning for hand gesture recognition. *Nat. Electron.* **4**, 54–63 (2021).
19. Lao, J. et al. Ultralow-power machine vision with self-powered sensor reservoir. *Adv. Sci.* **9**, 2106092 (2022).
20. Liao, F. et al. Bioinspired in-sensor visual adaptation for accurate perception. *Nat. Electron.* **5**, 84–91 (2022).
21. Jayachandran, D. et al. A low-power biomimetic collision detector based on an in-memory molybdenum disulfide photodetector. *Nat. Electron.* **3**, 646–655 (2020).
22. Choi, C. et al. Curved neuromorphic image sensor array using a MoS<sub>2</sub>-organic heterostructure inspired by the human visual recognition system. *Nat. Commun.* **11**, 5934 (2020).
23. Yu, J. et al. Bioinspired mechano-photonic artificial synapse based on graphene/MoS<sub>2</sub> heterostructure. *Sci. Adv.* **7**, eabd9117 (2021).
24. Park, H. L. et al. Retina-inspired carbon nitride-based photonic synapses for selective detection of UV light. *Adv. Mater.* **32**, e1906899 (2020).
25. Wang, H. et al. A ferroelectric/electrochemical modulated organic synapse for ultraflexible, artificial visual-perception system. *Adv. Mater.* **30**, e1803961 (2018).
26. Sun, L. et al. In-sensor reservoir computing for language learning via two-dimensional memristors. *Sci. Adv.* **7**, eabg1455 (2021).
27. Feng, G. et al. Flexible vertical photogating transistor network with an ultrashort channel for in-sensor visual nociceptor. *Adv. Funct. Mater.* **31**, 2104327 (2021).
28. Cui, B. et al. Ferroelectric photosensor network: an advanced hardware solution to real-time machine vision. *Nat. Commun.* **13**, 1707 (2022).
29. Yu, R. et al. Programmable ferroelectric bionic vision hardware with selective attention for high-precision image classification. *Nat. Commun.* **13**, 7019 (2022).
30. Pi, L. et al. Broadband convolutional processing using band-alignment-tunable heterostructures. *Nat. Electron.* **5**, 248–254 (2022).
31. Wu, G. et al. Programmable transition metal dichalcogenide homojunctions controlled by nonvolatile ferroelectric domains. *Nat. Electron.* **3**, 43–50 (2020).
32. Baugher, B. W. H., Churchill, H. O. H., Yang, Y. & Jarillo-Herrero, P. Optoelectronic devices based on electrically tunable p-n diodes in a monolayer dichalcogenide. *Nat. Nanotechnol.* **9**, 262–267 (2014).
33. Chen, P. et al. Approaching the intrinsic exciton physics limit in two-dimensional semiconductor diodes. *Nature* **599**, 404–410 (2021).
34. Xie, D. et al. Porous metal-organic framework/ReS<sub>2</sub> heterojunction phototransistor for polarization-sensitive visual adaptation emulation. *Adv. Mater.* **35**, e2212118 (2023).
35. Liu, K. et al. An optoelectronic synapse based on  $\alpha$ -In<sub>2</sub>Se<sub>3</sub> with controllable temporal dynamics for multimode and multiscale reservoir computing. *Nat. Electron.* **5**, 761–773 (2022).
36. Wu, G. et al. Hybrid MoS<sub>2</sub>/PbS quantum dots toward in-sensor reservoir computing. *IEEE Electron Device Lett.* **44**, 857–860 (2023).
37. Tong, L. et al. 2D materials-based homogeneous transistor-memory architecture for neuromorphic hardware. *Science* **373**, 1353–1358 (2021).
38. Bie, Y. Q. et al. A MoTe<sub>2</sub>-based light-emitting diode and photo-detector for silicon photonic integrated circuits. *Nat. Nanotechnol.* **12**, 1124–1129 (2017).
39. Wu, G. et al. MoTe<sub>2</sub> p-n homojunctions defined by ferroelectric polarization. *Adv. Mater.* **32**, e1907937 (2020).
40. Tian, B. B. et al. Tunnel electroresistance through organic ferroelectrics. *Nat. Commun.* **7**, 11502 (2016).
41. Chen, P., Peng, X. & Yu, S. 2017 IEEE International Electron Devices Meeting (IEDM) (IEEE, 2017).
42. Chen, P., Peng, X. & Yu, S. NeuroSim: a circuit-level macro model for benchmarking neuro-inspired architectures in online learning. *IEEE Trans. Comput.-Aided Design Integr. Circuits Syst.* **37**, 3067–3080 (2018).
43. Laughlin, S. B., de Ruyter van Steveninck, R. R. & Anderson, J. C. The metabolic cost of neural information. *Nat. Neurosci.* **1**, 36–41 (1998).
44. Liu, G. et al. Graphene-assisted metal transfer printing for wafer-scale integration of metal electrodes and two-dimensional materials. *Nat. Electron.* **5**, 275–280 (2022).
45. Liu, L. et al. Uniform nucleation and epitaxy of bilayer molybdenum disulfide on sapphire. *Nature* **605**, 69–75 (2022).
46. Kumar, S., Wang, X., Strachan, J. P., Yang, Y. & Lu, W. D. Dynamical memristors for higher-complexity neuromorphic computing. *Nat. Rev. Mater.* **7**, 575–591 (2022).

**Publisher's note** Springer Nature remains neutral with regard to jurisdictional claims in published maps and institutional affiliations.

Springer Nature or its licensor (e.g. a society or other partner) holds exclusive rights to this article under a publishing agreement with the author(s) or other rightsholder(s); author self-archiving of the accepted manuscript version of this article is solely governed by the terms of such publishing agreement and applicable law.

© The Author(s), under exclusive licence to Springer Nature Limited 2023, corrected publication 2023



## Methods

### Device and array fabrication

The bottom split gates with a 300 nm gap were fabricated by electron-beam lithography on a Si/SiO<sub>2</sub> (280 nm) substrate. The 250 nm P(VDF-TrFE) (70:30 mol%) layer was prepared using spin coating, followed by an annealing process at 135 °C for 6 h for high crystallinity. Few-layer MoTe<sub>2</sub> exfoliated from the bulk crystal was isolated onto a polydimethylsiloxane film and then transferred onto the P(VDF-TrFE) polymer. Before transferring onto MoTe<sub>2</sub> flakes, exfoliated graphene was etched into two flakes separated by a 10 μm gap using an oxygen-ion-etching process. Finally, Cr/Au (15/45 nm) was prepared using ultraviolet lithography and thermal evaporation. In the sensor array, the transferred Au electrodes are employed to substitute for graphene to enable scalable electrode preparation, followed by rapid thermal annealing at 100 °C for ohmic contacts. MoTe<sub>2</sub> is still mechanically exfoliated here.

### Device characterization

The Raman measurements were conducted using a HORIBA LabRAM HR800 instrument (532 nm laser). Electronic tests were performed with a commercial Keithley 4200A-SCS parameter analyser on a Lake Shore probe station under a vacuum at room temperature. A laser of 635 nm is used in the optoelectronic characterization process. In the sensor array, Columns 1, 4 and 7 are connected to produce the output of Array 1. Columns 2, 5 and 8 are connected to produce the output of Array 2. Columns 3, 6 and 9 are connected to produce the output of Array 3.

### Weight nonlinearity model

The device weight nonlinearity was described with the following model:

$$R_{\text{LTP}} = B \left( 1 - e^{-\frac{N}{A}} \right) + R_{\text{min}},$$

$$R_{\text{LTD}} = -B \left( 1 - e^{-\frac{N-N_{\text{max}}}{A}} \right) + R_{\text{max}},$$

$$B = (R_{\text{max}} - R_{\text{min}}) / \left( 1 - e^{-\frac{N_{\text{max}}}{A}} \right),$$

where  $R_{\text{LTP}}$  and  $R_{\text{LTD}}$  are the photoresponsivity in the LTP and LTD process, respectively. Experimental data  $R_{\text{max}}$ ,  $R_{\text{min}}$ ,  $N$  and  $N_{\text{max}}$  represent the maximum photoresponsivity, minimum photoresponsivity, number of voltage pulses and the maximum pulse number that switches the sensor between the minimum- and maximum-photoresponsivity states, respectively.  $A$  is a parameter that regulates the nonlinearity during weight update, which can be negative or positive.  $B$  is just a function of  $A$  that matches the function within the range of  $R_{\text{max}}$ ,  $R_{\text{min}}$  and  $N_{\text{max}}$ .

### Data availability

Source data are available via Figshare at <https://doi.org/10.6084/m9.figshare.24032001>. The data that support the plots within this

paper and other findings of this study are available from the corresponding authors upon reasonable request.

### Code availability

The code that supports the plots in this paper is available via GitHub at <https://github.com/zxmbrain/In-sensor-computing-with-dual-gates-devices>.

### Acknowledgements

This work is supported by the National Key Research and Development Program of China (grant no. 2021YFA1200700), National Natural Science Foundation of China (grant nos. T2222025, 62025405, 61825404, 61835012, 62104043, 62104044 and 62174053), the China National Postdoctoral Program for Innovative Talents (grant no. BX2021069), the China Postdoctoral Science Foundation (grant no. 2021M690649), Shanghai Science and Technology Innovation Action Plan (grant nos. 19JC141670, 21JC1402000 and 21520714100), Open Research Projects of Zhejiang Lab (2021MD0AB03) and Strategic Priority Research Program of Chinese Academy of Sciences (grant no. XDB44000000).

### Author contributions

G.W., X. Zhang, Q.L., B.T. and Jianlu Wang conceived the concept. Q.L., B.T. and Jianlu Wang supervised the research. G.W. and J.Z. fabricated the devices. Jingli Wang and M.Z. transferred the array Au electrode. G.W. and G.F. performed the electrical and optoelectronic measurements. X. Zhang, F.Z., C.Y. and K.Z. performed the edge detection and classification tasks. X. Zhang and D.D. designed the test program for the LTD and LTP processes. G.W., G.F., X. Zhao, D.G. and B.T. performed the chip-robot dog interaction video demo. C.D., J.C. and M.L. advised on the experiments and data analysis. All authors discussed the results and revised the manuscript.

### Competing interests

The authors declare no competing interests.

### Additional information

**Supplementary information** The online version contains supplementary material available at <https://doi.org/10.1038/s41563-023-01676-0>.

**Correspondence and requests for materials** should be addressed to Bobo Tian, Qi Liu or Jianlu Wang.

**Peer review information** *Nature Materials* thanks Yang Chai and the other, anonymous, reviewer(s) for their contribution to the peer review of this work.

**Reprints and permissions information** is available at [www.nature.com/reprints](http://www.nature.com/reprints).